LETTERS

# Coherent zero-state and π-state in an exciton–polariton condensate array

C. W. Lai[1,2,3], N. Y. Kim[1,2], S. Utsunomiya[3,4], G. Roumpos[1], H. Deng[1], M. D. Fraser[1], T. Byrnes[2,3], P. Recher[1,2], N. Kumada[4], T. Fujisawa[4] & Y. Yamamoto[1,3]

**The effect of quantum statistics in quantum gases and liquids results in observable collective properties among many-particle systems. One prime example is Bose–Einstein condensation, whose onset in a quantum liquid leads to phenomena such as superfluidity and superconductivity. A Bose–Einstein condensate is generally defined as a macroscopic occupation of a single-particle quantum state, a phenomenon technically referred to as off-diagonal long-range order due to non-vanishing off-diagonal components of the single-particle density matrix[1–3]. The wavefunction of the condensate is an order parameter whose phase is essential in characterizing the coherence and superfluid phenomena[4–11]. The long-range spatial coherence leads to the existence of phase-locked multiple condensates in an array of superfluid helium[12], superconducting Josephson junctions[13–15] or atomic Bose–Einstein condensates[15–18]. Under certain circumstances, a quantum phase difference of π is predicted to develop among weakly coupled Josephson junctions[19]. Such a meta-stable π-state was discovered in a weak link of superfluid $^3$He, which is characterized by a 'p-wave' order parameter[20]. The possible existence of such a π-state in weakly coupled atomic Bose–Einstein condensates has also been proposed[21], but remains undiscovered. Here we report the observation of spontaneous build-up of in-phase ('zero-state') and antiphase ('π-state') 'superfluid' states in a solid-state system; an array of exciton–polariton condensates connected by weak periodic potential barriers within a semiconductor microcavity. These in-phase and antiphase states reflect the band structure of the one-dimensional polariton array and the dynamic characteristics of metastable exciton–polariton condensates.**

The strong coupling between quantum well excitons and microcavity photons allows studies of cavity quantum electrodynamic effects in a solid-state system. The reversible energy exchange between the microcavity photons and quantum well excitons leads to the anti-crossing of eigenstates, known as the upper and lower exciton–polaritons (UPs and LPs)[22]. Unlike exciton–polaritons in bulk semiconductors, cavity exciton–polaritons involve no transport and are fully characterized by the in-plane wavenumber $k_{||}$, enabling a direct measurement of the exciton–polariton dispersion relation and momentum distribution of particles through angularly resolved spectroscopy[23]. The exciton–polaritons have been shown to condense in momentum space and exhibit spontaneous build-up of macroscopic spatial and temporal coherence[24–26]. Using Young's double-slit interference experiment, we measured a spatial coherence length of the condensate up to ~20 μm, limited by the pumping spot size (see Supplementary Information).

In our experiments, an array of one-dimensional cigar-shaped exciton–polaritons is created by the deposition of periodic strips of a metallic thin film on the top surface of the microcavity structure, as shown in Fig. 1a (see also Methods). The GaAs-based microcavity structure contains 12 quantum wells, exhibiting a vacuum Rabi splitting of ~14 meV. For the given microcavity structure under the metallic layer, the cavity resonance energy $E_C$ (for $k_{||} = 0$) is expected to increase by ~400 μeV according to the transfer matrix method[27]

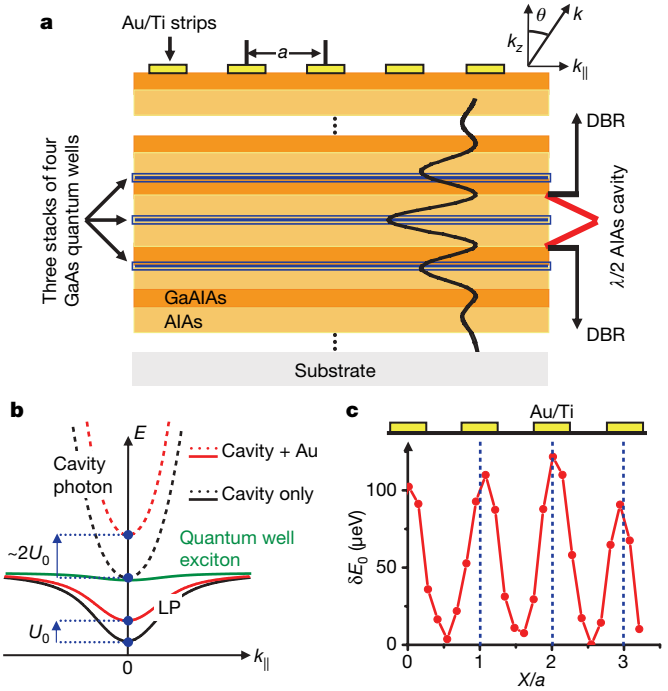


**Figure 1 | Formation of an exciton–polariton array. a**, A schematic of a cavity polariton array formed by depositing periodic thin metallic strips (Au/Ti) on top of a microcavity structure. The 1.4-μm-wide strips are equally spaced with a pitch distance $a = 2.8$ μm. The microcavity structure consists of a $\lambda/2$ AlAs cavity (indicated by red lines) sandwiched by two distributed Bragg reflectors with alternating GaAlAs/AlAs $\lambda/4$ layers, where $\lambda$ is the cavity resonance wavelength (varying around the quantum well exciton resonance, ~776 nm with tapering). Three stacks of four GaAs quantum wells are positioned at the central three antinodes of the microcavity photon field (the schematic black oscillatory curve). The distributed Bragg reflectors (DBR) consist of repeated GaAlAs/AlAs layers and are symbolized by the two short dotted vertical lines. **b**, Dispersion curves of the cavity photon mode (dashed lines) and LP (solid lines). The black dashed lines represent the uncoupled cavity photon mode and quantum-well heavy-hole exciton state, which are in resonance ($E_C = E_X$) at $k_{||} = 0$ in this case. The addition of the metallic layer shifts the LP energy (red solid line) by $U_0 \approx 200$ μeV. **c**, Spatial LP energy modulation $\delta E_0$ measured by scanning a pinhole across the lattice at the first conjugate real-image plane (see Fig. 2 and Methods).

[1]E. L. Ginzton Laboratory, Stanford University, Stanford, California 94305, USA. [2]Institute of Industrial Science, University of Tokyo, Meguro-ku, Tokyo 153-8505, Japan. [3]National Institute of Informatics, Hitotsubashi, Chiyoda-ku, Tokyo 101-8430, Japan. [4]NTT basic research laboratories, NTT Corporation, Atugi, Kanagawa 243-0198, Japan.

(see Methods). When the cavity photon ($E_C$) is near resonance with the quantum well exciton ($E_X$) at $k_{||} = 0$, the shift of the lower-polariton energy induced by the metallic layer is ~200 μeV, approximately half of the cavity photon resonance shift (Fig. 1b). Therefore, the LPs are expected to be trapped in the gap region where the LP energy is lower. The measured spatial modulation of LP energy is ~100 μeV, which is less than the theoretical prediction owing to the diffraction-limited spatial resolution (~2 μm) of our optical detection system (Fig. 1c). We confirm by an independent measurement that the LP energy in a bare microcavity is ~200 μeV lower than the LP energy under a uniform metallic layer of similar thickness for $E_C \approx E_X$.

The microcavity is excited by a mode-locked Ti:Sapphire laser with a ~2.5 ps pulse near the quantum well exciton resonance at an incident angle of 60°, corresponding to an in-plane wavenumber $k_{||} \approx 7 \times 10^4\ \mathrm{cm}^{-1}$ in air. The large $k_{||}$ of the pump ensures that the coherence of the pump laser is lost by multiple phonon emissions before the polaritons scatter into $k_{||} \approx 0$ states. The LP distributions in coordinate space (near-field) and momentum space (far-field) are measured by micro-photoluminescence spectroscopy and imaging, using the set-up shown in Fig. 2a (see Methods). The near-field images illustrate the spatial LP distribution, while the far-field images reveal the in-plane momentum LP distribution. The spectroscopy in momentum space (that is, angularly resolved spectroscopy) provides a direct measurement of the LP dispersion relation and effective mass.

For a system of two condensates, the interference fringes can be observed even in the absence of a locked relative phase in a single shot measurement[7]. In the case of an array of condensates, however, interference fringes appear only if the relative phases between consecutive condensates are locked[28]. The high degree of interference fringe visibility in momentum space can thus be used as an indication of a long-range spatial coherence across the whole array of multiple condensates. Such an interference measurement is commonly performed in atomic Bose–Einstein condensates by releasing condensates in an optical lattice.

Considering a periodic and coherent array of condensates aligned along the $x$ (where $x$ is $X$ or $Y$, see below) axis, we can approximate the order parameter in momentum space as[28]:

$$\psi(k_x) = \psi_0(k_x) \sum_{n=0,\pm 1 \ldots \pm n_M} e^{i n (k_x a + \phi)} = \psi_0(k_x) \frac{\sin(N k_x a/2)}{\sin(k_x a/2)}\bigg|_{\phi=0} \quad (1)$$

where $n$ labels the condensate array element, $N = 2n_M + 1$ is the total number of periodic array elements, $a$ is the pitch distance between two neighbouring elements, and $\psi_0(k_x)$ is the momentum-space wavefunction of an individual element. The overall momentum distribution, $\rho(k_x) = |\psi(k_x)|^2$, reflects the coherence properties and nature of the condensate arrays through distinctive interference patterns. In the presence of the lattice, the momentum distribution displays narrow peaks at $k_x = m \times 2\pi/a$ (where $m$ is an integer) with an envelope function given by $\rho_0(k_x) = |\psi_0(k_x)|^2$.

If all the elements are locked in-phase ($\phi = 0$), at a LP wavelength $\lambda = 780$ nm and a grating pitch distance $a = 2.8$ μm, a Fraunhofer diffraction pattern has a central peak at $\theta = 0°$ and two side lobes at $\theta = \sin^{-1}(\lambda/a) \approx \pm 16°$ ($k_{||} = \pm 2\pi/a$; $m = \pm 1$ first-order diffraction). The LP emissions from an exciton–polariton condensate array are expected to display such an interference pattern in momentum space, just like an atomic Bose–Einstein condensate experiment[15–18].

The observed LP distribution in both coordinate and momentum space of the condensate array are shown in Fig. 2b and c. Below the condensation threshold (pump power $P = 20$ mW), the near-field image reveals the cigar-shaped LP emissions through the 1.4-μm-wide gaps between the metallic strips. The corresponding LP momentum distribution is broad ($\Delta\theta_{FWHM} \approx 36°$) and isotropic, independent of the periodic intensity modulation and the elliptically shaped pumping spot. The result indicates that there is negligible phase coherence among different cigar-shaped LPs. With an increasing pumping rate, two strong and two weak side lobes emerge at

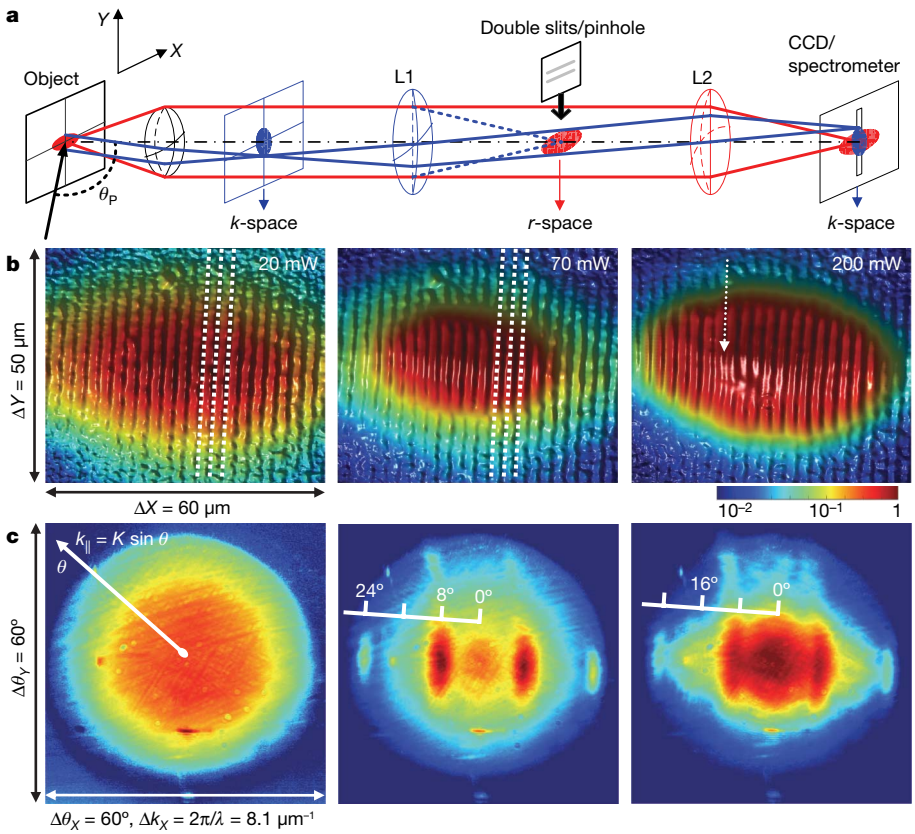


**Figure 2 | Imaging and spectroscopy of exciton–polariton distribution in coordinate and momentum space.** **a**, Schematic of the micro-photoluminescence set-up for imaging and spectroscopy in coordinate and momentum space (see Methods). $\theta_P \approx 60°$ is the incident angle of the pump beam. **b**, Near-field images showing the LP distribution across a polariton array in coordinate space under pumping powers of 20, 70 and 200 mW (left to right) at $T = 20$ K. Here the condensation threshold pumping power is ~45 mW (intensity ~1,600 W cm$^{-2}$). The white dashed lines indicate selected locations of the 1.4-μm-wide metallic strips. The colour scale is the normalized LP emission intensity. **c**, Corresponding far-field images showing the LP distribution in momentum space. When passing through the threshold, lobes at ±8° and ±24° emerge out of the isotropic background of the thermal polariton gas, which is indicative of the π-state. The strong central lobe at 0° and two weak lobes at ±16° appear at higher pumping rates, indicative of the zero-state.

$\theta \approx \pm 8^\circ$ and $\pm 24^\circ$, which correspond to $k_{||} = \pm \pi/a$ and $k_{||} = \pm 3\pi/2a$, respectively. The diffraction pattern suggests that the phase difference of adjacent condensates in the array is locked exactly to $\pi$ (see $\phi = \pi$ in equation (1)). Moreover, the corresponding near-field image (in Fig. 2b; 70 mW) reveals that strong LP emissions are generated from under the metallic strips rather than the gaps. The contrast is better observed near the boundary of the central condensate and the outside thermal LP emissions, which come through the gaps. The dominant LP emission through the metallic layers despite the lower transmission indicates that LP condensates are strongly localized under the metallic strips. With a further increasing pumping rate, the intensity of the central peak near $\theta = 0^\circ$ with weak side lobes at $\theta \approx \pm 16^\circ$ (Fig. 2c) gradually surpasses the peaks at $\theta \approx \pm 8^\circ$ and $\pm 24^\circ$ as shown in Fig. 2c. The corresponding near-field image of the condensate also recovers a standard spatial modulation (near the central area indicated by the white arrow in Fig. 2b).

These two distinct interference patterns suggest the transition from an antiphase state to an in-phase state. We refer to the in-phase state as the 'zero-state' and the antiphase state as the 'π-state' on the basis of their relative phase differences between adjacent elements.

Both the zero-state and π-state can be observed for an exciton–polariton condensate array consisting of more than 30 strips of condensates (total array dimension ~100 μm). These collective states are manifestations of the long-range spatial coherence as well as of phase-locking across the array. Next, we examine the phase-locking mechanism for the zero-state and π-state through the LP dispersion relation.

In Fig. 3a, we show the energy versus in-plane momentum spectra for an LP array near resonance $E_C \approx E_X$ and below threshold. From the dispersion curve, we deduce the LP kinetic energy at $k_{||} = \pm G_0/2 = \pi/a$ (half of the primitive reciprocal lattice vector), $E_k = \hbar^2 (G_0/2)^2 / 2m^* \approx 500$ μeV, where the LP effective mass $m^* = 9 \times 10^{-5} m_e$ (where $m_e$ is the free electron mass). The kinetic energy $E_k$ is larger than the spatial LP energy modulation, $U_0 \approx 200$ μeV. Therefore, we expect the exciton–polariton condensate to be only weakly perturbed by the periodic potential and the coherence is maintained across the array. In such a large tunnelling limit, we neglect the polariton–polariton interaction and deduce the band structure of the polariton array by assuming a 'nearly free polariton' in the presence of the periodic square-well potential. Given a one-dimensional periodic potential $U_0(X)$ with a lattice constant $a$, the band structure can be obtained using the standard Bloch wavefunction formalism. Only those polaritons with in-plane momentum close to the Bragg condition ($k_{||} = m\,G_0/2$) are subject to backscattering, owing to the periodic potential, and gaps appear at the Bragg planes where standing waves are formed. Similar to the standard extended-zone scheme[29], the band structure can be constructed by starting with an original parabola and displaced parabolas $E_{LP}(k_{||} \pm mG_0)$, as shown in Fig. 3b. Here the size of the circles represents the expected relative LP emission intensity from each band (Methods). We observe this in the LP energy versus in-plane momentum with a below-threshold pumping rate (Fig. 3a). The first bandgap, between the first and second bands near the zone boundaries (Bragg planes), is of the order of the barrier potential, $|U_0|$. This small gap is masked in the measured spectra by the large inhomogeneous broadening of the LP emission lines (linewidth ~500 μeV).

In Fig. 3c, we show the energy versus in-plane momentum of a polariton condensate array above threshold and $E_C - E_X \approx +6$ meV. Above threshold, LP emissions occur in two states with an energy difference of about 1 meV. These two states with emission peaks at $k_{||} = 0, \pm G_0$ and at $k_{||} = \pm G_0/2, \pm 3G_0/2$ correspond to the zero-state and π-state, respectively.

On referring to the multi-valley band structure (Fig. 3b), the dynamic condensation process of the exciton–polariton array becomes more transparent. Without the spatial modulation, the quasi-stationary state of the LP condensate is the lowest-energy state at $k_{||} = 0$. Here the bottom of the LP dispersion parabola serves as a 'trap' of polaritons in momentum space. When the spatial potential modulation is introduced, a meta-stable dynamic condensate can occur near the bottom of the second band (point A in Fig. 3b). At these points, polaritons experience a relaxation bottleneck, resulting in metastable condensates. Eventually, the LP system will relax to the lowest-energy in-phase state (point C in Fig. 3b) as the pumping rate is increased.

To understand the spatial distributions of LPs in the array (near-field images shown in Fig. 2b), we consider the Bloch wavefunctions. The Bloch wavefunctions for these eigenstates exhibit not only opposite relative phases between adjacent elements in the array but also different characteristics. Schematic Bloch wavefunctions for selected eigenstates labelled as A, B and C in Fig. 3b are shown in Fig. 3d. The zero-state at point C corresponds to the 's-like' state with maximal amplitude in potential wells and identical phase between adjacent elements across the array. The wavefunctions of A and B at $k_{||} = G_0/2$ both exhibit a relative π-phase difference between adjacent elements. The lower-energy state at point B corresponds to anti-bonding of 's-states', while the higher-energy state at point A corresponds to bonding of 'p-states'. Like the atomic p-state, the LP density vanishes at the centre of the potential well for this π-state. This is fully confirmed by the near-field imaging shown in Fig. 2b. We note that under the weak potential modulation, the Bloch wavefunctions are superpositions of forward-and-backward travelling plane waves at the zone boundary and have a relatively broad distribution in space compared to the standard tight-binding model of a normal condensed-matter system.

The metastability of the π-state is a unique property for dynamic polariton condensates. Under strong pumping rates, the zero-state dominates eventually, owing to enhanced cooling by stimulated polariton–polariton scattering at high densities. A typical evolution

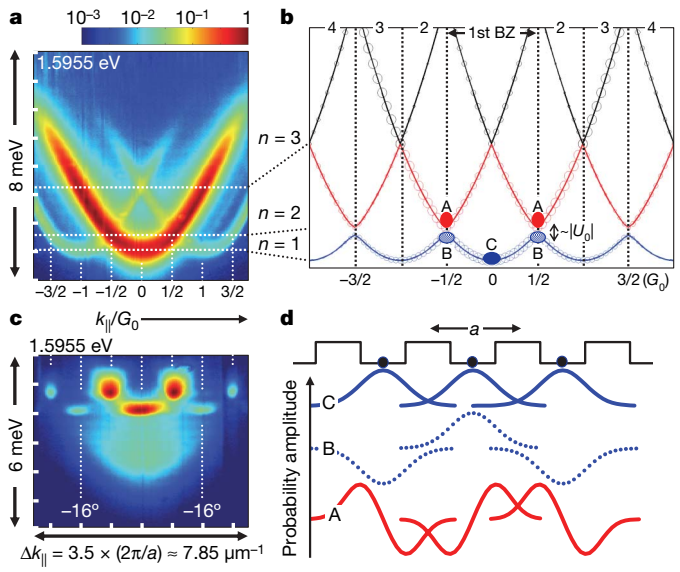


**Figure 3 | Band structure and 'superfluid' states in an exciton–polariton condensate array. a**, Time-integrated energy versus in-plane momentum ($E$ versus $k_{||}$) near resonance $E_C \approx E_X$ below threshold ($P = 10$ mW) at $T \approx 7$ K. The central bright parabola corresponds to the dispersion curve for the polaritons in the absence of a periodic potential. Two additional parabolas displaced by $\pm G_0 = \pm 2\pi/a$ cross the central dispersion curve at $k_{||} = \pm G_0/2$. **b**, Extended-zone scheme of the band structure. Anti-crossing occurs at the boundary between the first and second Brillouin zones (BZ). The size of the open circles represents the expected relative emission intensity (log scale) of each energy band. Condensation occurs at the valleys labelled by solid red (point A) and blue (point C) circles. **c**, $E$ versus $k_{||}$ at blue detuning $E_C - E_X \approx 6$ meV above threshold ($P = 40$ mW). The lobes at $k_{||} = 0, \pm G_0$ correspond to the in-phase zero-state, whereas the lobes at $k_{||} = \pm G_0/2$, $\pm 3G_0/2$ correspond to the antiphase π-state. **d**, Schematic Bloch-wave functions for states labelled as A, B or C in **b**.

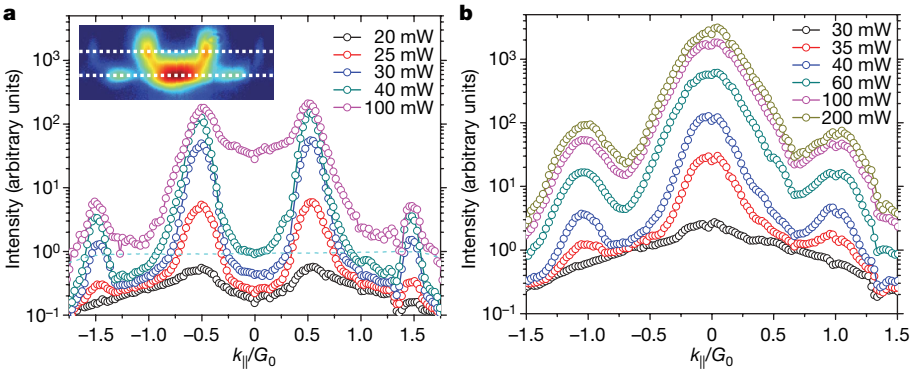


**Figure 4 | Evolution of the 'zero-state' and 'π-state'. a**, Profiles of the π-state as a function of in-plane momentum taken at a cross-section in the dispersion curve (exemplified by the white dotted lines in the inset) for an exciton–polariton condensate array for various pumping rates. The inset shows the energy versus in-plane momentum spectra (axes and colour scale same as Fig. 3c, but only the top 2 meV is shown in the inset) for $P = 100$ mW, where relaxation from the π-state to zero-state is visible. The blue dashed line displays the uniform collection efficiency of the optical system up to $|k_{||}| = 3G_0/2$. **b**, Profiles of the zero-state. The intensity of the zero-state surpasses that of the π-state at around $P = 45$ mW.

from the metastable π-state to the stationary zero-state is illustrated by the LP momentum distribution profiles for various pumping rates in Fig. 4. At a high pumping rate, the LP emission from the zero-state surpasses that from the π-state by more than an order of magnitude. The transition between these dynamic condensates depends on the coupling strength between adjacent elements in the array (see Supplementary Information).

Thus we observed a metastable condensate in a π-state (anti-bonding of p-states) as well as a stable condensate in a zero-state (bonding of s-states) in an exciton–polariton array. Such a coherent linear superposition state formed over many condensates in periodical sites is referred to as a 'superfluid' state. However, some common superfluidity properties such as the frictionless flow over a long distance beyond the pumping region are not necessarily meant. Our experiments constitute a first step towards the experimental study of a dynamical Bose–Hubbard model in a solid-state system. The polariton system allows the direct observation of the spatial and momentum distributions as well as the dispersion characteristics of the condensates. For instance, full control of the on-site interaction, barrier potential and occupation number may allow us to study the dynamical quantum phase transition properties of a Mott insulator.

## METHODS SUMMARY

The periodic spatial modulation of LP energy ~200 μeV is induced by the periodic thin metallic strips (a ~20-nm-thick Au /3-nm-thick Ti layer) with a pitch distance $a = 2.8$ μm deposited on top of the microcavity. The relative transmission through the top distributed Bragg reflectors (DBR) with and without the metallic layer is ~40–50%.

The imaging and spectroscopy of LPs in the near-field (coordinate space) and far-field (momentum space) are performed by positioning a charged-coupled-device (CCD) camera or an imaging spectrometer in a plane conjugate to the real-image or Fourier (back focal) plane of the objective. The collection efficiency is approximately uniform to a full angle of ~60°.

More details about the preparation of the metallic grating layer and its effects on the far-field interference pattern, the experimental settings, including the determination of the in-plane wavevector in momentum space, and the expected LP diffraction patterns and intensities of the zero-state and π-state are given in the Methods section and Supplementary Information.

**Full Methods** and any associated references are available in the online version of the paper at www.nature.com/nature.

**Received 23 May; accepted 20 September 2007.**

1. Penrose, O. & Onsager, L. Bose-Einstein condensation and liquid helium. *Phys. Rev.* **104,** 576–584 (1956).
2. Beliaev, S. T. Application of the methods of quantum field theory to a system of bosons. *J. Exp. Theor. Phys.* **34,** 417–432 (1958).
3. Yang, C. N. Concept of off-diagonal long-range order and the quantum phases of liquid He and of superconductors. *Rev. Mod. Phys.* **34,** 694–704 (1962).
4. Tilley, D. R. & Tilley, J. *Superfluidity and Superconductivity* Chs 1–3, and 7 (Adam Hilger, New York, 1990).
5. Pitaevskii, L. P. & Stringari, S. *Bose-Einstein Condensation* (Clarendon, Oxford, 2003).
6. Leggett, A. J. *Quantum Liquids: Bose Condensation and Cooper Pairing in Condensed-matter Systems* Chs 1–4 (Oxford Univ. Press, Oxford, 2006).
7. Andrews, M. R. *et al.* Observation of interference between two Bose condensates. *Science* **275,** 637–641 (1997).
8. Hagley, E. W. *et al.* Measurement of the coherence of a Bose-Einstein condensate. *Phys. Rev. Lett.* **83,** 3112–3115 (1999).
9. Bloch, I., Hansch, T. W. & Esslinger, T. Measurement of the spatial coherence of a trapped Bose gas at the phase transition. *Nature* **403,** 166–170 (2000).
10. Castin, Y. & Dalibard, J. Relative phase of two Bose-Einstein condensates. *Phys. Rev. A.* **55,** 4330–4337 (1997).
11. Naraschewski, M. & Glauber, R. J. Spatial coherence and density correlations of trapped Bose gases. *Phys. Rev. A.* **59,** 4595–4607 (1999).
12. Davis, J. C. & Packard, R. E. Superfluid $^3$He Josephson weak links. *Rev. Mod. Phys.* **74,** 741–773 (2002).
13. Hansen, J. B. & Lindelof, P. E. Static and dynamic interactions between Josephson junctions. *Rev. Mod. Phys.* **56,** 431–459 (1984).
14. Hadley, P. M., Beasley, R. & Wiesenfeld, K. Phase locking of Josephson-junction series arrays. *Phys. Rev. B* **38,** 8712–8719 (1988).
15. Cataliotti, F. S. *et al.* Josephson junction arrays with Bose-Einstein condensates. *Science* **293,** 843–846 (2001).
16. Anderson, B. P. & Kasevich, M. A. Macroscopic quantum interference from atomic tunnel arrays. *Science* **282,** 1686–1689 (1998).
17. Orzel, C. *et al.* Squeezed states in a Bose-Einstein condensate. *Science* **291,** 2386–2389 (2001).
18. Greiner, M. *et al.* Quantum phase transition from a superfluid to a Mott insulator in a gas of ultracold atoms. *Nature* **415,** 39–44 (2002).
19. Bulaevskii, L. N., Kuzii, V. V. & Sobyanin, A. A. Superconducting system with weak coupling to current in ground state. *JETP Lett.* **25,** 290–294 (1977).
20. Backhaus, S. *et al.* Discovery of a metastable pi-state in a superfluid $^3$He weak link. *Nature* **392,** 687–690 (1998).
21. Smerzi, A. *et al.* Quantum coherent atomic tunneling between two trapped Bose-Einstein condensates. *Phys. Rev. Lett.* **79,** 4950–4953 (1997).
22. Weisbuch, C. *et al.* Observation of the coupled exciton-photon mode splitting in a semiconductor quantum microcavity. *Phys. Rev. Lett.* **69,** 3314–3317 (1992).
23. Houdre, R. *et al.* Measurement of cavity-polariton dispersion curve from angle-resolved photoluminescence experiments. *Phys. Rev. Lett.* **73,** 2043–2046 (1994).
24. Deng, H. *et al.* Polariton lasing versus photon lasing in a semiconductor microcavity. *Proc. Natl Acad. Sci. USA* **100,** 15318–15323 (2003).
25. Deng, H. *et al.* Quantum degenerate exciton-polaritons in thermal equilibrium. *Phys. Rev. Lett.* **97,** 146402 (2006).
26. Kasprzak, J. *et al.* Bose-Einstein condensation of exciton polaritons. *Nature* **443,** 409–414 (2006).
27. Yeh, P. *Optical Waves in Layered Media* Ch. 5 (John Wiley, Hoboken, 2005).
28. Pedri, P. *et al.* Expansion of a coherent array of Bose-Einstein condensates. *Phys. Rev. Lett.* **87,** 220401 (2001).
29. Madelung, O. *Introduction to Solid-state Theory* Ch. 2 (Springer, Berlin, 1996).

**Supplementary Information** is linked to the online version of the paper at www.nature.com/nature.

**Acknowledgements** This work was supported by the JST/SORST programme and by Special Coordination Funds for Promoting Science and Technology in Japan. The high-quality microcavity cavity sample is courtesy of G. S. Solomon, R. Hey, K. Ploog and A. Forchel. We thank T. Maruyama for support and S. Sasaki for the device fabrication. C.W.L. thanks Y. R. Shen for comments and discussions.

**Author Information** Reprints and permissions information is available at www.nature.com/reprints. Correspondence and requests for materials should be addressed to C.W.L. (cwlai@stanford.edu) or Y.Y. (yyamamoto@stanford.edu).

## METHODS

**Exciton–polariton array.** The thin metallic film deposited on top of the microcavity modifies the boundary condition of the top DBR structure. For a bare microcavity structure, the resonant photon mode exhibits an anti-node at the semiconductor/free-space interface. In the presence of a metallic layer, the anti-node shifts towards the centre of the cavity, owing to suppression of the electromagnetic field inside the metallic layer. As a result, the energy of the cavity photon resonance increases (blue shift). For a 20-nm-thick Au/3-nm-thick Ti layer on top of the microcavity structure, the cavity resonance energy increases by ~400 μeV according to the calculation by the transfer matrix method[27]. The associated LP energy shift is of the order of ~200 μeV near-resonance $E_C \approx E_X$, approximately half of the cavity resonance shift. This is consistent with the experimentally measured energy shift under a uniform metallic layer of similar thickness.

The relative transmittance through the top DBR with and without the metallic layer is ~40–50%, so the optical pumping and LP emission through the periodic metallic strips are spatially modulated. The initial spatial modulation of LP generation by the metallic strips is mostly washed out by internal diffusion of polaritons through the cooling process. However, the detected LP emission is subject to intensity modulation by the periodic metallic strips. This effect must be separately considered for understanding the far-field interference pattern from the spontaneously formed 'zero-state' and 'π-state' under the built-in periodic potential.

**Experimental techniques.** The exciton–polaritons are excited by a p-polarized Ti:sapphire laser of 2.5 ps duration (0.5 meV spectral width) at a 76 MHz repetition rate. The pulses are focused to an elliptical spot (~60 μm × 30 μm or ~100 μm × 50 μm) onto the sample at an oblique incidence angle of ~60° ($k_{||} \approx 7 \times 10^4\,\mathrm{cm}^{-1}$ in air). The elliptical pumping spot covers approximately 20–30 periodic elements.

LPs are trapped in the cavity mostly until they relax to states of lower energy and in-plane momentum. The emitted luminescence is collected by a micro-photoluminescence set-up composed of a 50× objective lens (effective focal length, $f_{obj} = 4$ mm and a numerical aperture, NA = 0.55, corresponding to a full collection angle of ~67° in air) and a pair of relay lenses of focal length $f_L = 10$ cm (L1, which is removable, and L2) as shown in Fig. 2. The collection efficiency is approximately uniform up to a full angle $\Delta\theta \approx 60^\circ$ ($\Delta k_{||} \approx 2\pi/\lambda$).

The imaging and spectroscopy of LPs in the near-field (coordinate space) and far-field (momentum space) are performed by positioning a charged-coupled-device (CCD) camera or an imaging spectrometer in a plane conjugate to the real-image or Fourier (back focal) plane of the objective. The optical axis of the collection optical system is perpendicular to the surface of the sample. For imaging and spectroscopy in coordinate space (near-field), the repositionable lens L1 is removed. The Fourier (back focal) plane of the sample located in the object plane, with coordinates X and Y, is thus imaged onto to a CCD camera directly or through an imaging spectrometer. This arrangement allows determination of the LP distribution in momentum space ($k_X$, $k_Y$) (far-field imaging) as well as the LP dispersion relation $E_{LP}(k_{||})$. Coordinate space is correlated to momentum space by a Fourier transform: $(X, Y) = (u/M, v/M) \leftrightarrow (k_X, k_Y) = \left(k \times u/f_{obj}, k \times v/f_{obj}\right)$, where $M$ is the magnification ($M = f_L/f_{obj} \approx 25$), ($u$, $v$) are coordinates of the near-field or far-field images, and $k_{||} = k_{X,Y} = k \sin\theta = (2\pi/\lambda)\sin\theta$ in air. Near-field and far-field images are measured with a CCD with a pixel size of $\sim 8 \times 8\,\mu\mathrm{m}^2$, giving a diffraction-limited spatial resolution of ~2 μm and a pixel-size-limited angular resolution of $\delta\theta = 0.11^\circ$. The energy versus in-plane momentum relation of LPs and LP arrays are determined by spectroscopy in momentum space (angle-resolved spectroscopy). The spectroscopic system is a 75-cm spectrometer equipped with an 1,800 g mm$^{-1}$ grating and a liquid-nitrogen-cooled CCD with a pixel size of $26 \times 26\,\mu\mathrm{m}^2$. The system has an angular resolution of $\delta\theta \approx 0.4^\circ$ and a spectral resolution of ~20 μeV, limited by the pixel size.

**LP emission intensity from the array.** The probability amplitude of LPs in the presence of a periodic potential is represented by the Bloch wave function $\psi_{n,k_{||}}$, where $k_{||}$ is the in-plane lattice momentum, and $n$ the index of the band. The expected leakage LP emission intensity is proportional to the overlapping probability density $\rho = \left|\left\langle \phi_{k_{||}} | \psi_{n,k_{||}} \right\rangle\right|^2$, where $\phi_{k_{||}} = \exp\left[i k_{||} \cdot r\right]$ is the plane wave corresponding to the free-moving polaritons (that is, photons leaking out from the cavity) with in-plane momentum $k_{||}$. The calculated relative $\rho$ of each energy band is represented by the size of the open circles (log scale) in Fig. 3b.